

Preparation and properties of thin amorphous tantalum films formed by small e-beam evaporators

Kevin Stella¹, Damian Bürstel¹, Steffen Franzka¹, Oliver Posth² and Detlef Diesing¹

¹ Fachbereich Chemie, Universität Duisburg-Essen, D-45117 Essen, Germany

² Experimentalphysik, Universität Duisburg-Essen, D-47048 Duisburg, Germany

E-mail: detlef.diesing@uni-due.de

Received 7 January 2009, in final form 5 May 2009

Published 19 June 2009

Online at stacks.iop.org/JPhysD/42/135417

Abstract

Large area ($A = 6 \text{ cm}^2$), thin tantalum films ($5 \text{ nm} < d < 100 \text{ nm}$) are accomplished by evaporation from tantalum rods using small pocket e-beam evaporators. Using a sample to source distance of $\approx 20 \text{ cm}$, homogeneous amorphous films with a small surface roughness ($< 1 \text{ nm}$) can be prepared on glass. Films are characterized by scanning electron microscope images, atomic force microscopy, electrochemical oxidation and resistivity measurements as a function of film thickness. The samples show high resistivities of $200\text{--}2000 \mu\Omega \text{ cm}$. The temperature coefficient of the resistivity (TCR) is negative, as characteristic for highly disordered metals. A theoretical description of the thickness distribution (evaporation from plane and hemispherical sources on plane targets) is given in the appendix.

1. Introduction

Thin tantalum films and contacts may play a key role in future micro- and nanoelectronic devices due to their high stiffness and corrosion resistance [1–4]. For this reason, the preparation of thin tantalum films seems to be of continuing interest despite the vast literature in the last four decades [5–12]. These earlier works were mainly focused on the macroscopic properties of the films. A comprehensive review of the early period handling, in particular, the main preparation methods sputtering and electron evaporation with bent beams can be found in Westwood's book [13].

The interesting and sometimes confusing point concerning tantalum as well as niobium and tungsten films is the allotropy. These films appear in simple body centred configurations as well as in tetragonal phases [14]. Also phase transitions may appear [15]. Both configurations of tantalum can be produced in sputter deposition processes. A nearly completely amorphous modification of tantalum films can be produced by pulsed laser deposition [16].

The different phases of tantalum show distinct differences in their electrical resistivities:

- Low resistivity ($10\text{--}60 \mu\Omega \text{ cm}$) α -tantalum in body centred cubic phase [17, 18].
- High resistivity ($100\text{--}200 \mu\Omega \text{ cm}$) β -tantalum in the tetragonal phase [12, 14, 19, 20].
- Completely amorphous films ($> 200 \mu\Omega \text{ cm}$) [16].

The crystalline modifications of thin tantalum films can be used for bonding and electric conduction whereas the amorphous modification takes on a special position. Their application field is located more in mechanical applications due to their elastic strain limit and fracture toughness [21].

This work attempts to show that an amorphous modification of tantalum can be expected, when films are e-beam evaporated on simple glass substrates. The appearance of the amorphous structure is surprising since comparable experiments with sputtered tantalum films on glass substrates lead to polycrystalline samples [1, 22]. The difference may be caused by the existence of ions and particles with higher kinetic energy in the sputter process [23], whereas in the e-beam setup

presented here, a large sample–source distance of around 20 cm suppresses the contribution of ions.

The structure of the samples is investigated by scanning electron microscopy (SEM) and atomic force microscopy (AFM). These techniques reveal that our films show a continuous smooth structure and suggest an amorphous modification of the tantalum.

However, the discrimination between a nanocrystalline and an amorphous structure is difficult by means of microscopy techniques only. Therefore, resistivity measurements as a function of film thickness are used to characterize the overall conduction mechanism up to thicknesses of 100 nm. These experiments are combined with measurements of the temperature coefficient of the resistivity (TCR). This method was often applied to nitride and oxide films of tantalum [1, 24]. In this work the method is applied to an elemental tantalum film to determine the amorphous structure of the tantalum film in the context of Tsuei's and Mooij's theory of electronic transport in strongly disordered metals [25, 26].

2. Experimental

2.1. Electron beam evaporation

A commercial e-beam evaporator (TECTRA) is used in our experiments. The filament (a tungsten wire of 0.5 mm thickness) is heated by a current density of $2 \times 10^3 \text{ A m}^{-2}$. Between the filament wire and the tantalum rod (distance $\approx 5 \text{ mm}$) a voltage $U = 1.3 \text{ kV}$ is applied. The resulting field strength E can be estimated at $E = 1.3 \text{ kV}/5 \text{ mm} \approx 2.6 \times 10^5 \text{ V m}^{-1}$, which is clearly below the breakdown field strength $E_{\text{DB}} = (1.5\text{--}2.6) \times 10^8 \text{ V m}^{-1}$ of tungsten filaments under vacuum conditions [27]. The electron current emitted from the filament is measured at the tantalum rod (emission current).

The 3 mm thick rod forms a tantalum sphere with a radius of 3 mm at the top of the rod (see figure 1). Under the simplified assumption of a homogeneous electron current on the hemisphere of the molten tantalum one can estimate the necessary current density j_e for the evaporation by the ratio of the emission current I_e during evaporation and the hemisphere's surface (see figure 1) by $j_e = I_e / (\frac{1}{2} \cdot 4 \cdot \pi \cdot r^2)$ to $2 \times 10^3 \text{ A m}^{-2}$.

Since the voltage on the tantalum is kept constant, the dissipated power is simply $P = U \cdot j_e$, which is a value of $2.6 \times 10^6 \text{ W m}^{-2}$ in our case. The vapour pressure p in torr of the tantalum [13, 28] is given by the temperature T in kelvin:

$$p = 10^{11.1 - (47000 \cdot K/T)} \text{ Torr.} \quad (1)$$

The path of the evaporating tantalum atoms intersects with the path of the electrons. This leads to a partial ionization of the atomic beam. Some of these ionized atoms impinge the flux electrode, which is an isolated electrode mounted on the front end of the e-beam evaporator. The tantalum ions cause a small current, which is in the range $1\text{--}2 \mu\text{A}$. Assuming a constant ionization rate, control of the tantalum atom flux is possible by monitoring the tantalum ion current at the flux electrode. The distance between the top of the flux monitor electrode at the

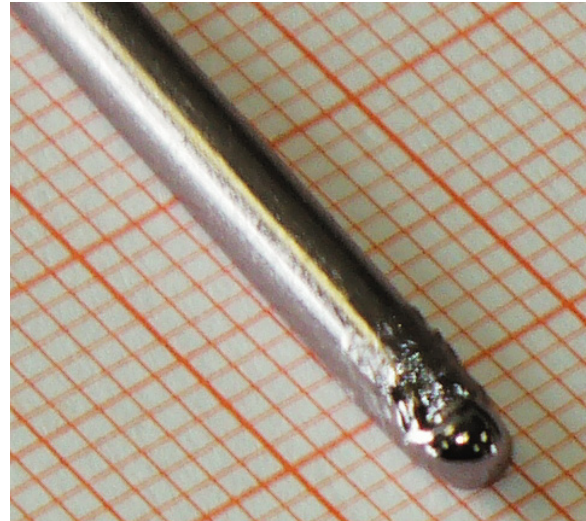


Figure 1. Photo of the tantalum rod. The hemisphere (diameter $\approx 3 \text{ mm}$) due to the evaporation can be seen on the right side at the top of the rod.

end of the electron beam evaporator and the substrate surface is 178 mm.

The diameter of the flux electrodes aperture is 6 mm, which is 3 mm larger than the diameter of the tantalum hemisphere. There is a clear line-of-sight from the whole hemisphere to the substrate. Thus, a simple treatment of the evaporator as a Knudsen type effusion cell is not sufficient. A derivation of the thickness distribution caused by ample evaporation sources (planar and hemispherical sources) will be given in the appendix.

A quartz microbalance is mounted just besides the sample. The substrates were isopropanol cleaned microscope glass slides. The evaporation rate was fixed to 0.4 nm min^{-1} for all samples.

2.2. Tantalum film characterization

2.2.1. Characterization of the tantalum film by SEM. In figure 2 SEM images of the evaporated films with 20 and 100 nm thickness are shown. No structures are observable on the 20 nm sample. Small structures (approximate size 5–10 nm) can only be seen on the 100 nm sample. We did not investigate thicker films of, for example, 500 nm thickness. It would be interesting whether there is a thickness induced change to a more polycrystalline structure. A thickness induced change in the sample structure cannot be excluded since Zhou and coworkers show quite big structures and grains on 500 nm thick tantalum films [1]. But these samples contain 20 at% oxygen. The oxygen contents of our samples were determined by time of flight secondary ion mass spectrometry (TOF SIMS) to be below 1% [29].

Hence, we think that especially for the thickness range $\leq 40 \text{ nm}$ our images point to a homogeneous (maybe even amorphous) structure with a small roughness which contains elemental tantalum only. The homogeneous structure will be verified in the next section by AFM investigations.

The question, whether there is a thickness induced change in the film morphology from amorphous tantalum to crystalline

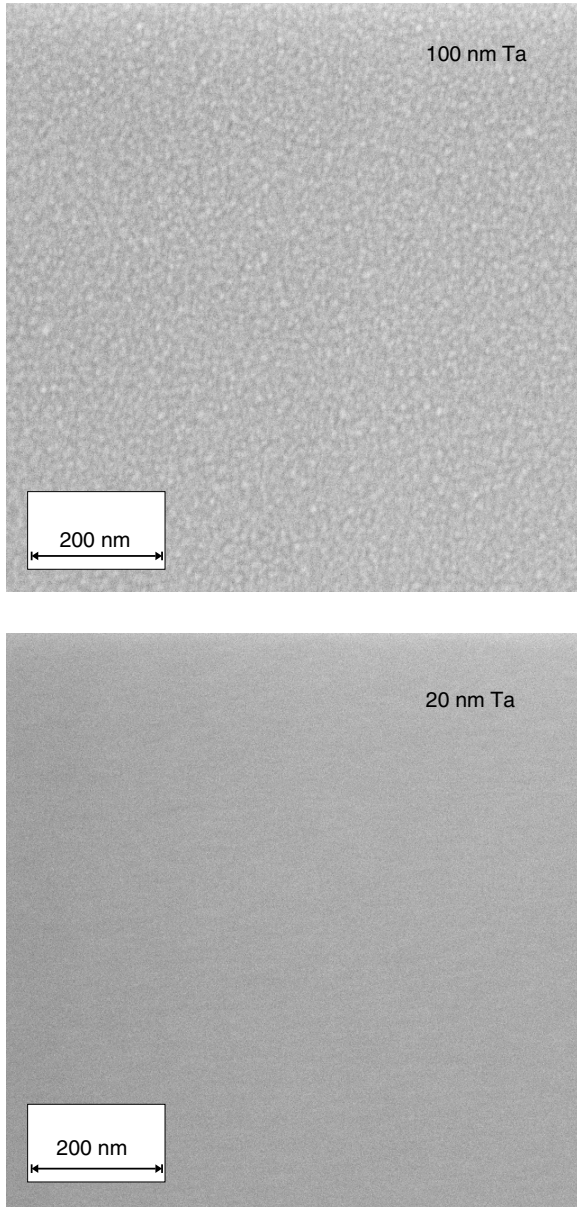


Figure 2. Scanning electron microscopy images of 100 and 20 nm thick tantalum films. Magnification: 2×10^5 .

modifications for films thicker than 100 nm with negligible oxygen contents must be left open for the moment and will be addressed in a later work [30].

2.2.2. Characterization of the tantalum film by AFM. AFM investigations were performed for 10, 20, 40 and 100 nm thick films. As suggested by the SEM images only small roughness values can be detected. The linescans (a)–(c) in figure 3 show roughness values below 1 nm. Only the scan for the 100 nm sample shows a roughness value of around 2 nm. It should be noted that the roughness shown in our AFM line scans of around 1 nm is clearly smaller than the values reached for sputtered tantalum films on glass of around 10 nm [1].

In figure 4 an AFM-topography of the tantalum is shown for the 20 nm thick sample. It confirms the absence of any overlaid macroscopic structure on a $5 \mu\text{m}$ scale.

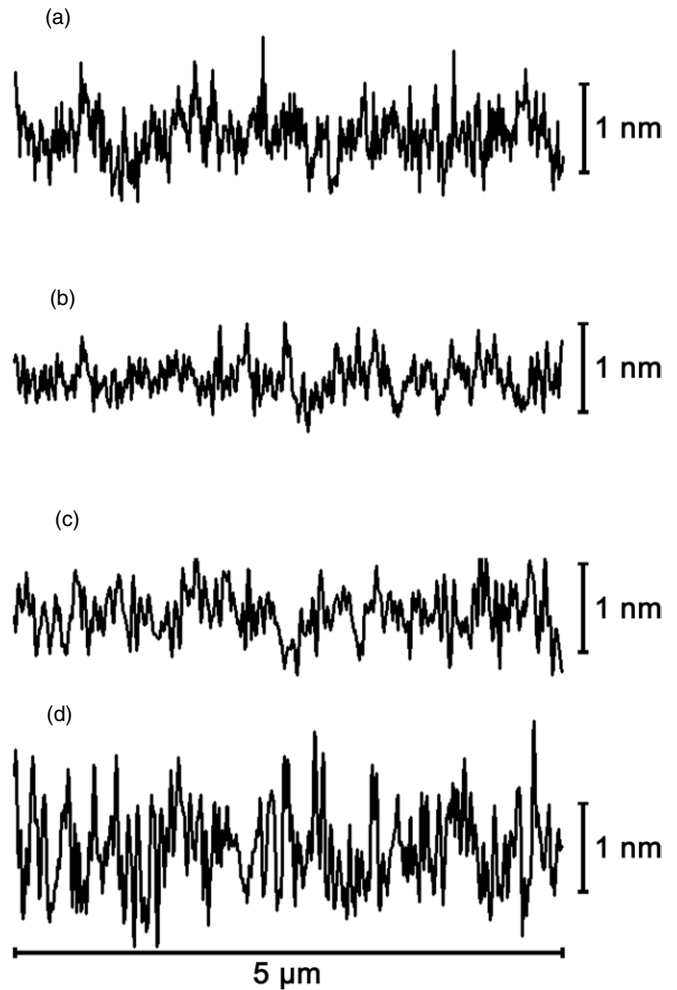


Figure 3. AFM linescans on 10, 20, 40 and 100 nm thick tantalum films (a)–(d).

Apparently the AFM and SEM investigations point to a very smooth structure (for the 10–40 nm samples) with only a small structure change for the 100 nm sample.

However, both methods cannot distinguish between nanocrystalline structures (diameter $< 2 \text{ nm}$) and a completely amorphous film. Some further hints for a prevalent amorphous structure will be given by resistivity measurements in a later section.

For a crosscheck we performed x-ray-diffraction measurements in θ – 2θ geometry. The scan did not show any peaks, only a broad maximum at around $2\theta = 25^\circ$ could be seen. This also points to a completely disordered structure.

The determination of the tantalum film thicknesses by AFM needs a special preparation of the film, since an atomic force microscope needs localized sharp edges (scan range $\approx 10 \mu\text{m}$). The scratching of thin tantalum films with metals, for example steel needles, does not harm the metal with modest pressure. With higher pressures the metal can be removed, but damages in the underlying glass cannot be excluded.

Therefore, a different procedure for the formation of sharp edges in tantalum films has to be applied. We use a commercial permanent marker to produce a thin line on the glass substrate, which acts as a spacer layer between tantalum and glass in

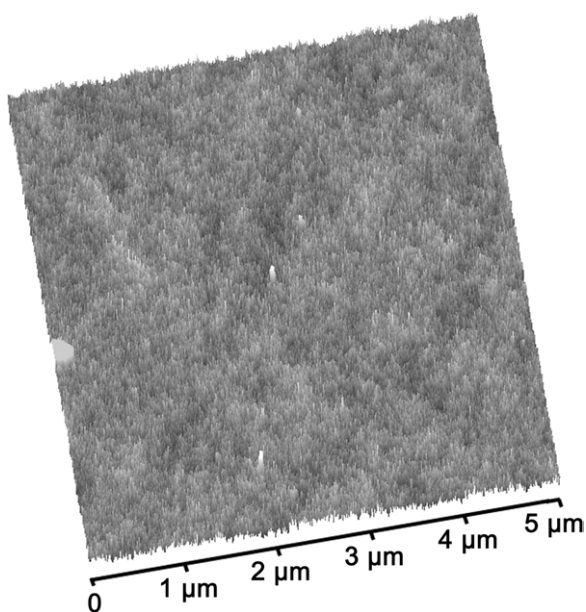


Figure 4. Topography of the tantalum film.

the course of the evaporation process. After the evaporation procedure, the polymer of the marker with the weakly bound tantalum layer on top can be easily wiped off with an ethanol wetted tissue (see figure 5). This procedure produces an extremely sharp edge, comparable to a breaking edge in a crystal without modifying the other parts of the sample (see figure 6). All thickness values used in this work are gauged by AFM height measurements accomplished on the edges of the tantalum films prepared by this method.

2.3. Growth of tantalum films on silicon

In addition we performed SEM and x-ray-diffraction measurements of tantalum thin films on n-doped Si(111) wafers. Both experimental methods yield similar results as for the tantalum–glass system. The SEM did not show any structures. In the XRD no line besides the substrate induced line at $2\theta = 27^\circ$ could be observed.

Therefore, we can exclude that the growth of amorphous tantalum films is a specific property of the tantalum–glass interface.

2.4. Electrochemical characterization of the tantalum film

Thin metal films can be characterized with respect to their homogeneity and mechanical stability by an electrochemical oxidation procedure. Single crystals and smooth homogeneous tantalum films show after the onset potential a constant oxidation current when the electrochemical potential is increased linearly with time [31–33]. An example for a freshly prepared tantalum film is shown in the upper view graph of figure 7. An initial potential of -1.2 V is applied. At this potential no chemical reaction occurs. Then the potential is increased with a rate of 0.1 V s^{-1} up to a final value of $E_{\text{final}} = 1.8$ V. At around -0.3 V (denoted as $E_{1/2}$ —half wave potential) a considerable current increase is

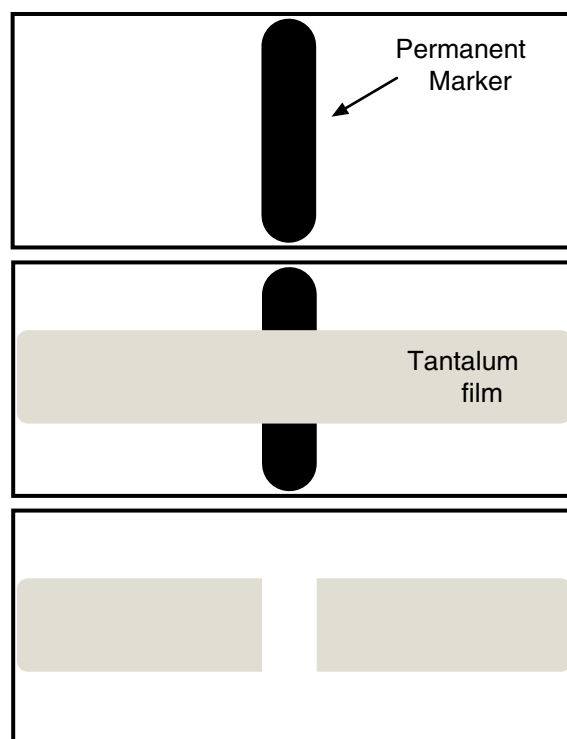


Figure 5. Upper view graph: scheme of the permanent marker line on the glass substrate. Middle view graph: tantalum film evaporated above the marker on the glass substrate. Bottom view graph: after removing the marker line with an ethanol wetted tissue, this part of the tantalum film can be peeled off.

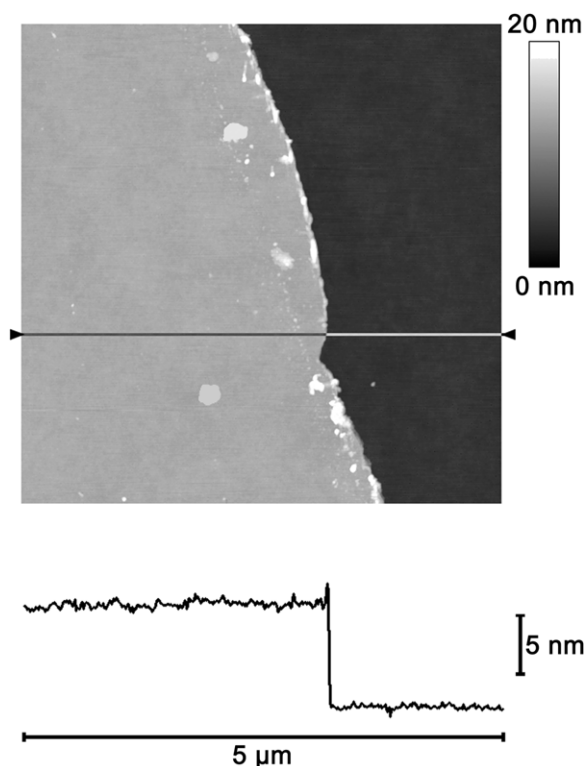


Figure 6. Upper view graph: topography across the sharp edge of the film. Lower view graph: AFM linescan across the sharp edge of the film.

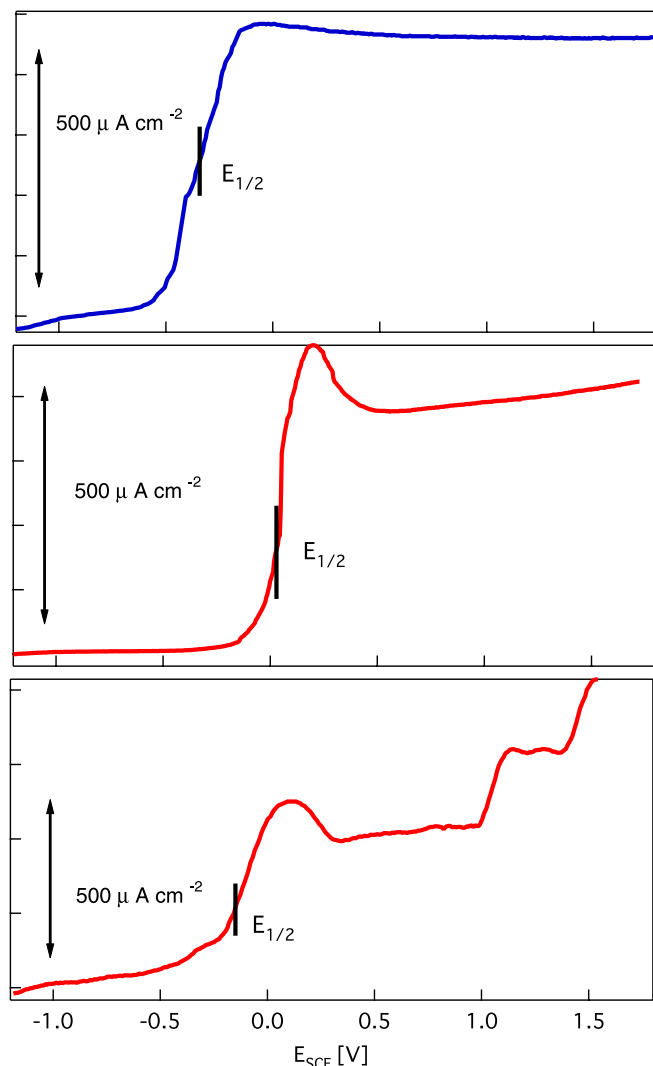


Figure 7. Cyclic voltammograms of tantalum films ($E_{\text{initial}} = -1.2 \text{ V}$, $E_{\text{final}} = +1.8 \text{ V}$, $dE/dt = 0.1 \text{ V s}^{-1}$). Straight lines denote the half wave potential $E_{1/2}$. Upper view graph: freshly prepared film. Middle view graph: tantalum film exposed to ambient conditions for 10 h. Bottom view graph: tantalum film including a dust enclosure.

monitored, followed by a constant current density of around $500 \mu\text{A cm}^{-2}$. When the electrode potential is stopped at the final value of 1.8 V , the current drops exponentially to zero within a few seconds. The potential driven chemical reaction occurring on the tantalum film is a pure oxidation. Parallel processes as corrosion can be neglected since the oxide has a negligible solubility in the sodium acetate buffer electrolyte used here [34]. Under these conditions it is known that the final value of the built oxide layer scales linearly with E_{final} [34].

In figure 7 the middle view graph shows a cyclic voltammogram of a tantalum film, which was exposed to ambient conditions for 10 h. One can see the delayed current increase (corresponding to a shift of $E_{1/2}$ of $+0.35 \text{ V}$) which is due to a previous oxidation of the tantalum by ambient oxygen. The mentioned shift corresponds to a thickness increase of 0.7 nm [35]. Increasing the potential further leads to a constant current density of around $500 \mu\text{A cm}^{-2}$ as well. When the final value of 1.8 V is reached and kept constant, the current drops

exponentially as a function of time similar to the experiment mentioned above.

In the bottom view graph a cyclic voltammogram of a site on the tantalum film with a dust enclosure is shown. Up to a potential of -0.2 V the experimental curve looks quite similar to the curves in the upper and middle graph. But at a potential of $E \approx 1.0 \text{ V}$ a considerable current increase is monitored, followed by a second one at 1.5 V . When the potential is held constant at -1.8 V , the current does not simply fall exponentially to zero as in the previous experiments, but shows several sudden current spikes. After the end of the oxidation this film shows mechanical cracks whereas the samples with smooth cyclic voltammograms do not show any visible modifications.

The reason for this oxidation behaviour can be seen in the strong mechanical tension of the oxidized metal which is due to the volume increase [36, 37]. Discontinuities as dust enclosures then tend to break up. The break up will supply new, unoxidized metal to the electrolyte. This is most probably the reason for the sudden current increases in the bottom view graph of figure 7.

XPS sputter profiles were taken from the anodically oxidized samples. Incorporated cations (sodium in this case) could not be found in the oxide layer. The oxygen contents of the tantalum film itself were found to be below 1% [38].

3. Electrical resistivity of thin tantalum films

Furthermore, the tantalum films were characterized by measurements of their electric resistivity. The setup for the resistivity measurements in this section (using 2 mm wide and 2 cm long stripes) was described elsewhere [31]. In the upper view graph of figure 8 the specific resistivity ρ of the tantalum film is plotted as a function of the film thickness d . The values are calculated with the resistance R of the samples by

$$\rho = R \cdot \frac{d \cdot b}{l}, \quad (2)$$

where l is the length and b the width of the sample ($l = 20 \text{ mm}$, $b = 2 \text{ mm}$). This simplified approach is meaningful only if the topography of the film does not change significantly with the film thickness [39, 40]. However, this seems to be at least partly fulfilled for these samples as shown in figures 2 and 3. The observed values lying in the range of some $100 \mu\Omega \text{ cm}$ (red crosses in upper view graph of figure 8) are around 100 times higher than the value for bulk tantalum at room temperature ($\rho = 13.4 \mu\Omega \text{ cm}$ [41], see black line (c) in upper view graph of figure 8).

The high resistivity values observed here are even higher than the values for liquid tantalum. In the liquid phase tantalum shows a specific resistivity of $80\text{--}150 \mu\Omega \text{ cm}$ [42] and $85\text{--}120 \mu\Omega \text{ cm}$ [43]. Both value ranges can be seen as horizontal boxes ((a) and (b) in the upper view graph of figure 8). In sum, these results point to a structure of the tantalum films showing even a higher disorder than a liquid.

To exclude surface effects or size effects due to the limited thickness of the films, the resistivity data are analysed

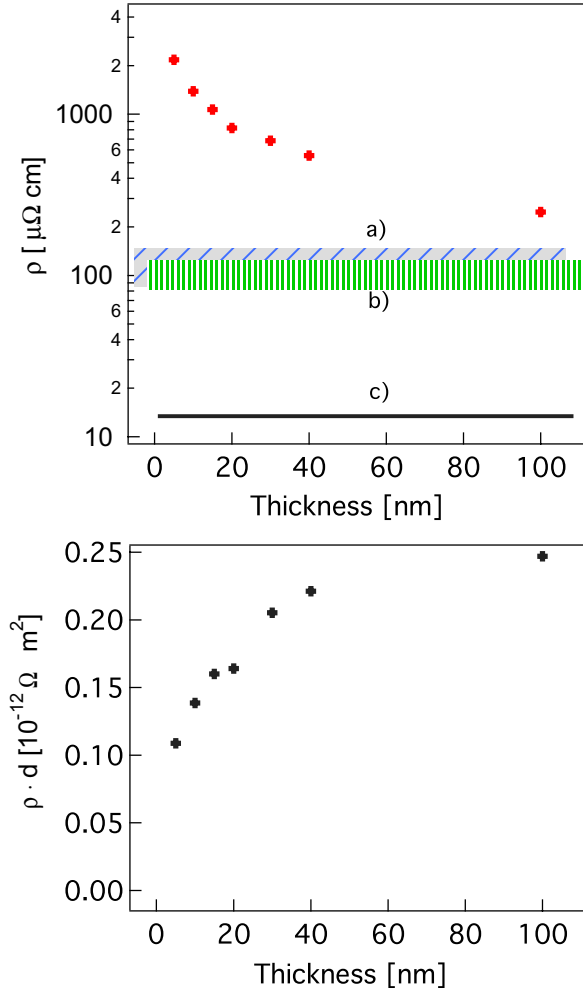


Figure 8. Upper view graph: specific resistivity ρ (red crosses) of the tantalum films as a function of the film thickness. Values of ρ for molten tantalum (boxes (a)) and (b)) according to [42] and [43], respectively. Horizontal line (c) denotes the value for bulk tantalum [41]. Lower view graph: product of specific resistivity ρ and film thickness d as a function of d .

with the classical Fuchs–Sondheimer approximation [20, 44] according to

$$\rho \cdot d = \rho_{\infty} \cdot d + \frac{3}{8} \rho_{\infty} l_{\infty} \cdot (1 - p), \quad (3)$$

where ρ_{∞} is the resistivity of an infinitely thick film with the same structure as the investigated film. l_{∞} is the analogously defined mean free path and p the specularity parameter (fraction of electrons being mirror-like reflected at the film interfaces). A $\rho \cdot d$ versus d plot is shown in the lower view graph of figure 8. One can clearly see that there is no linear behaviour. Hence, the resistivity of the tantalum films cannot be described within the Fuchs–Sondheimer approach.

A further indicator for a disordered structure is the TCR. This value $\alpha(\rho)$ is commonly evaluated by [26]

$$\alpha(\rho) = \frac{1}{\rho} \cdot \frac{d\rho}{dT}. \quad (4)$$

α can be expected to be positive for crystalline films, whereas it should be negative for amorphous tantalum films [16].

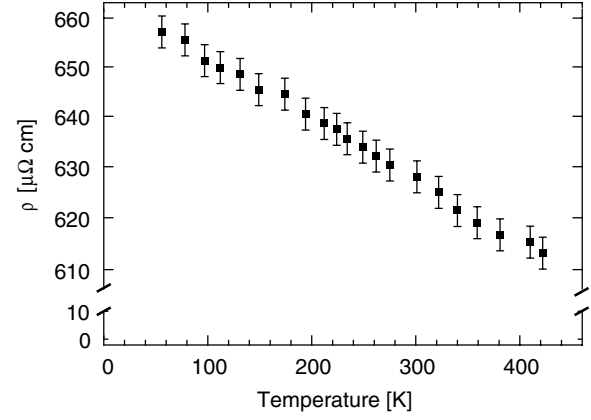


Figure 9. Temperature dependence of a 40 nm thick tantalum film.

Following the theory of Mooij and Tsuei [25, 26], one can expect high negative $\alpha(\rho)$ values for specific resistivities $\rho > 500 \mu\Omega \text{ cm}$. For this reason we show the temperature dependent resistivity of a 40 nm thick tantalum film (ρ at 300 K $\approx 630 \mu\Omega \text{ cm}$) in figure 9. This sample shows a reproducible linear decrease in the resistivity when cooled from 450 to 60 K. From the slope one can get negative TCR values (typically -2.3×10^{-4} and $-2.1 \times 10^{-4} \text{ 1/K}$ for 15 and 40 nm thick films) according to equation (4).

These results are in good agreement with the data collected by Tsuei [26]. For 15 and 40 nm thick films (specific resistivities of $1066 \mu\Omega \text{ cm}$ and $630 \mu\Omega \text{ cm}$, see figure 8) the values of $\alpha(\rho)$ are definitely negative (similar to investigations on pulsed laser deposited tantalum [16]). This coincidence and the homogeneous smooth structure of our films lets us assign our negative α values to an intrinsic property of the electron transport in amorphous tantalum.

4. Conclusion

In this work we showed how thin amorphous tantalum films can be prepared by small e-beam evaporators. With a distance of $\approx 20 \text{ cm}$ between source and sample homogeneous films with thickness variations below 1% can be achieved.

The SEM images, AFM investigations and the resistivity measurements point to a completely amorphous and smooth structure of the thin tantalum films (grown on glass and silicon substrates). This result is supported by the negative TCR of $\approx -2 \times 10^{-4} \text{ 1/K}$ of the thin films, which is in coincidence with the literature values for highly disordered metals.

Despite their amorphous character the adhesion of tantalum on glass slides is strong. Therefore, the films cannot be peeled off easily. The fixing of the film thickness by AFM measurements across a sharply defined tantalum edge is possible with a classical ‘lift off’ procedure. The surface of the films was found to be quite smooth (less than 1 nm roughness). Due to their high hardness and adhesive power on the glass, the tantalum films can be reproducibly modified by an electrochemical oxidation procedure without any cracks or mechanical damages. Scalable oxide thicknesses up to 4 nm can be accomplished by oxidation potentials up to 2 V.

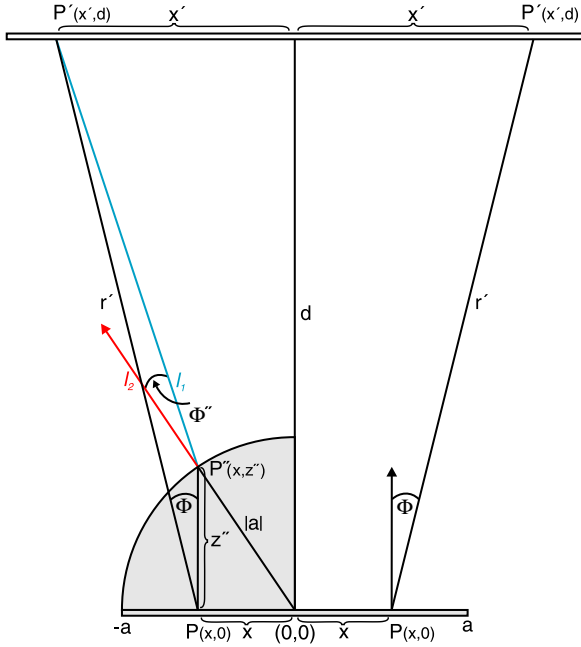


Figure 10. Comparison of the geometries for evaporation from a planar evaporation source (right side) and from a hemispherical evaporation source (left side).

The smooth and continuous structure of the thin films allows their application in the manufacturing of heterojunctions. These can be metal–insulator–metal structures [45, 46] as well as the application in stacked metals [47]. Furthermore, very thin and stiff cover layers (also for use in STM) may be formed with these films. With respect to biocompatibility elemental amorphous tantalum might be of advantage over alloys [48].

Acknowledgments

This work is supported by the Deutsche Forschungsgemeinschaft in the frame of the SFB 616 ‘Energy Dissipation Processes on Surfaces’. KS wishes to thank the ‘Studienstiftung des deutschen Volkes’ for support. The authors wish to thank Katrin Bruder and Achim W Hassel (Max-Planck-Institute Düsseldorf) and Günter Dumpich for stimulating discussions. Skilful technical assistance by tectra GmbH Physikalische Instrumente in Frankfurt/Main is acknowledged.

Appendix. Theoretical description of film thickness distribution: comparison of plane and hemispherical sources

In this appendix we give a short description of the film thickness distribution caused by evaporation from ample sources. Figure 10 shows on the right-hand side the geometry for evaporation from a planar evaporation source of width $2a$, whereas the left-hand side shows the geometry for hemispherical sources such as a molten rod with radius a .

The target plane is at a distance d from the source plane. On the source plane the coordinates are unprime notations in

the case of a planar source or double prime notations when the considered point of the evaporation is on the hemisphere’s surface. On the target plane the coordinates are in prime notations. The differential mass flux $d\Phi_{P'}/dx$ on a point $P'(x', d)$ caused by evaporation from the point $P(x, 0)$ is proportional to $(r')^{-2}$ and $\cos(\phi)$ where $r' = \sqrt{(x' - x)^2 + d^2}$ [49–51]. With $\cos(\phi) = d/r'$ one gets

$$\begin{aligned} \frac{d\Phi_{P'}}{dx} &= C \cdot \frac{1}{r'^2} \cdot \cos(\phi) \\ &= C \cdot \frac{1}{(x' - x)^2 + d^2} \cdot \frac{d}{\sqrt{(x' - x)^2 + d^2}}. \end{aligned} \quad (5)$$

Considering a planar evaporation source of width $2a$ one gets the total mass flux $\Phi_{P'}$ on P' caused by the whole evaporation source as

$$\Phi_{P'} = \frac{C}{2a} \int_{-a}^a \frac{d}{((x' - x)^2 + d^2)^{3/2}} dx. \quad (6)$$

In the case of evaporation from a molten rod, having a hemisphere with the radius a on top, one has to consider a simple transformation of coordinates. The point $P(x, z = 0)$ on the source plane moves to the point $P''(x, z'')$ of the hemisphere’s surface. So the transformations for $P \rightarrow P''$ are

$$\begin{aligned} x &\rightarrow x'' & x &= x'', \\ z = 0 &\rightarrow z'' & z'' &= \sqrt{a^2 - x^2}. \end{aligned}$$

The total mass flux at $P(x', d)$ can be formulated in this case analogously to equation (5):

$$\Phi_{P'} = \frac{C}{2a} \int_{-a}^a \frac{\cos(\phi'')}{((x' - x'')^2 + (d - z'')^2)} dx. \quad (7)$$

One has to consider that the cosine-like evaporation profile on P'' must be calculated with respect to the surface normal in P'' . Hence, ϕ in equation (5) has to be transformed in ϕ'' in equation (7).

ϕ'' is the included angle of the straight lines l_1 and l_2 (see figure 10). l_2 is the surface normal in P'' , l_1 is the straight line $P' - P''$. The slopes of the two lines are $(z'' - d)/(x - x')$ for l_1 and z''/x for l_2 . The included angle can then be calculated by

$$\phi'' = \frac{\pi}{2} - \left(\arctan \left(\frac{z'' - d}{x - x'} \right) + \arctan \left(\frac{z''}{x} \right) \right). \quad (8)$$

Replacing of ϕ'' in equation (7) by equation (8) allows the direct comparison of the thickness distribution on a flat sample caused by a molten rod with one caused by a planar evaporation source using equation (6).

In figure 11 the results for planar and hemispherical sources are compared for targets close to (lower view graph) and far (upper view graph) from the evaporation source (for example $a = 1.5$ mm and $d = 15$ mm or 150 mm, respectively). The constant C in the previous equations is set to 1, because it does not change the thickness distribution. The range of the x -axis is chosen to be three times the radius of the source. The mass flux is plotted relative to the value

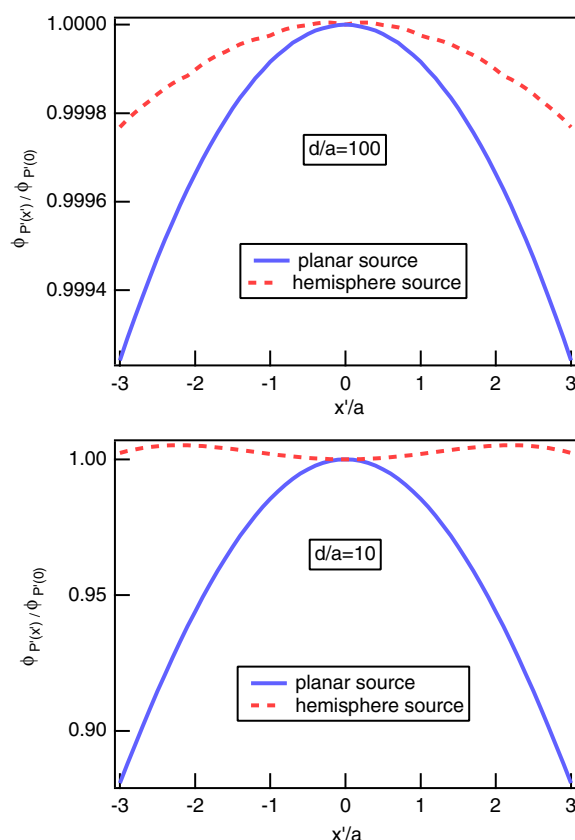


Figure 11. Calculated thickness distribution for a hemispherical evaporation source and for a planar evaporation source. Upper view graph: ratio of distance to radius of the evaporation source $d/a = 100$. Lower view graph: $d/a = 10$.

on the centre axis at $x = 0$. In the upper view graph for $d/a = 100$ one can see that the planar and the hemispherical source show a negligible thickness distribution of below 1%. This changes for distances close to the source (lower view graph). For $d/a = 10$ the thickness distribution gets much more pronounced for planar sources. A decrease of up to 12% is calculated for the planar source. In contrast, the hemispherical source shows a much lower variation in the thickness distribution. Additionally, the hemispherical source shows pronounced maxima at $x \approx 2.2 \cdot a$. This leads to the sometimes observed corona-like thickness distributions. The maxima and the corresponding local minimum at $x = 0$ are due to the projection of the hemisphere's cosine distributions on the flat target plane.

In sum, the hemispherical sources produce more homogeneous thickness distributions for close as well as distant targets.

References

- [1] Zhou Y M, Xie Z, Xiao H N, Hu P F and He J 2008 *Vacuum* **83** 286–91
- [2] Guziewicz M, Piotrowska A, Kaminska E, Graszka K, Diduszko R, Stonert A, Turos A, Sochacki M and Szmids J 2006 *Mater. Sci. Eng. B* **135** 289–93
- [3] Zhang M, Yang B, Chu J and Nieh T G 2006 *Scr. Mater.* **54** 1227–30
- [4] Zhang M, Zhang Y F, Rack P D, Miller M K and Nieh T G 2007 *Scr. Mater.* **57** 1032–5
- [5] Liu L, Wang Y and Gong H 2001 *J. Appl. Phys.* **90** 416–20
- [6] Gerstenberg D and Calbick C J 1964 *J. Appl. Phys.* **35** 402–7
- [7] Baker P N 1972 *Thin Solid Films* **14** 3–25
- [8] Baker P N 1971 *Thin Solid Films* **8** R3–R3
- [9] Westwood W D and Livermore F C 1971 *Thin Solid Films* **8** R1–R2
- [10] Feinstein L G and Huttemann R D 1974 *Thin Solid Films* **20** 103–14
- [11] Feinstein L G and Huttemann R D 1973 *Thin Solid Films* **16** 129–45
- [12] Feinstein L G and Gerstenberg D 1972 *Thin Solid Films* **10** 79–89
- [13] Westwood W D, Waterhouse N and Wilcox P S 1975 *Tantalum Thin Films* (London: Academic)
- [14] Nnolim N O, Tyson T A and Axe L 2003 *J. Appl. Phys.* **93** 4543–60
- [15] Lee S L, Windover D, Lu T M and Audino M 2002 *Thin Solid Films* **420–421** 287–94
- [16] Narayan J, Bhosle V, Tiwari A, Gupta A, Kumar P and Wu R 2006 *J. Vac. Sci. Technol. A: Vac. Surf. Films* **24** 1948–54
- [17] Zhang J Q, Huai Y M, Chen L F and Zhang J 2003 *J. Vac. Sci. Technol. B* **21** 237–40
- [18] Valletti K, Subrahmanyam A and Joshi S V 2008 *Surf. Coat. Technol.* **202** 3325–31
- [19] Schwartz N, Reed W A, Polash P and Read M H 1972 *Thin Solid Films* **14** 333–46
- [20] Sajovec F, Meuffels P M and Schober T 1992 *Thin Solid Films* **219** 206–9
- [21] Johnson W 2002 *JOM J. Min. Met. Mater. Soc.* **54** 40–3
- [22] Hassel A W 2009 private communications
- [23] Dalla Torre J, Gilmer G H, Windt D L, Kalyanaraman R, Baumann F H, O'Sullivan P L, Sapjeta J, Diaz de la Rubia T and Djafari Rouhani M 2003 *J. Appl. Phys.* **94** 263–71
- [24] Na S-M, Park I-S, Park S-Y, Jeong G-H and Suh S-J 2008 *Thin Solid Films* **516** 5465–9
- [25] Mooij J H 1973 *Phys. Status Solidi* **17** 521–30
- [26] Tsuei C C 1986 *Phys. Rev. Lett.* **57** 1943–6
- [27] Ahearn A J 1936 *Phys. Rev.* **50** 238–53
- [28] Honig R E 1962 *RCA Rev.* **23** 567
- [29] Bruder K, Hassel A W, Stella K, Diesing D and Mardare A 2009 in preparation
- [30] Stella K and Diesing D 2009 in preparation
- [31] Stella K and Diesing D 2007 *J. Electrochem. Soc.* **154** C663–70
- [32] Macagno V and Schultze J W 1984 *J. Electroanal. Chem.* **180** 157–70
- [33] Mozalev A, Smith A J, Borodin S, Plihaika A, Hassel A W, Sakairi M and Takahashi H 2009 *Electrochim. Acta* at press
- [34] Schultze J W and Hassel A W 2003 *Encyclopedia of Electrochemistry* vol 4, section 3.2 (Weinheim: Wiley-VCH) pp 216–70
- [35] Schultze J W and Lohrengel M M 2000 *Electrochim. Acta* **45** 2499–513
- [36] Rosenband V and Gany A 1995 *Corros. Sci.* **37** 1991–2001
- [37] Sankaranarayanan S K R S and Ramanathan S 2008 *Phys. Rev. B* **78** 085420
- [38] Bruder K, Stella K, Diesing D and Hassel A W, unpublished results
- [39] Reiss G, Vancea J and Hoffmann H 1986 *Phys. Rev. Lett.* **56** 2100–3
- [40] Hoffmann H and Vancea J 1981 *Thin Solid Films* **85** 147–67
- [41] Lide D R (ed) 1996 *CRC Handbook of Chemistry and Physics* (London: CRC) pp 12–41, chapter 12
- [42] Berthault A, Arles L and Matricon J 1986 *Int. J. Thermophys.* **7** 167
- [43] Pottlacher G and Seifert A 2002 *Int. J. Thermophys.* **23** 1281
- [44] Sondheimer E H 1952 *Adv. Phys.* **1** 1–42

- [45] Jeliarzova Y, Kayser M, Mildner B, Hassel A W and Diesing D 2006 *Thin Solid Films* **500** 330
- [46] Mildner B, Hasselbrink E and Diesing D 2006 *Chem. Phys. Lett.* **432** 133
- [47] Jackson W B *et al* 2006 *J. Non-Cryst. Solids* **352** 859–62
- [48] Prigent H, Pellen-Mussi P, Cathelineau G and Bonnaureh-Mallet M 1998 *J. Biomed. Mater. Res.* **39** 200–6
- [49] Knudsen M 1917 *Ann. Phys. Lpz.* **357** 105–8
- [50] Knudsen M 1916 *Ann. Phys. Lpz.* **353** 1113–21
- [51] Matsushima T 2007 *Prog. Surf. Sci.* **82** 435–77